On-Orbit Geometric Calibration of ZY-3 Three-Line Array Imagery With Multistrip Data Sets

Yongjun Zhang, Maoteng Zheng, Jinxin Xiong, Yihui Lu, and Xiaodong Xiong

Abstract—ZY-3, which was launched on January 9, 2012, is the first stereo mapping satellite in China. The initial accuracy of direct georeferencing with the onboard three-line camera (TLC) imagery is low. Sensor geometric calibration with bundle block adjustment is used to improve the georeferencing accuracy. A new on-orbit sensor calibration method that can correct the misalignment angles between the spacecraft and the TLC and the misalignment of charge-coupled device is described. All of the calibration processes are performed using a multistrip data set. The control points are automatically matched from existing digital ortho map and digital elevation model. To fully evaluate the accuracy of different calibration methods, the calibrated parameters are used as input data to conduct georeferencing and bundle adjustment with a total of 19 strips of ZY-3 TLC data. A systematic error compensation model is introduced as the sensor model in bundle adjustment to compensate for the position and attitude errors. Numerous experiments demonstrate that the new calibration model can largely improve the external accuracy of direct georeferencing from the kilometer level to better than 20 m in both plane and height. A further bundle block adjustment with medium-accuracy ground control points (GCPs), using these calibrated parameters, can achieve external accuracy of about 4 m in plane and 3 m in height. Higher accuracy of about 1.3 m in plane and 1.7 m in height can be achieved by bundle adjustment using high-accuracy GCPs.

Index Terms—Bundle block adjustment, direct georeferencing, interior orientation parameters (IOPs), multistrip, on-orbit geometric calibration, three-line camera (TLC), ZY-3.

I. INTRODUCTION

THREE-LINE array image technology was first applied in the Modular Optoelectronic Multispectral Stereo Scanner during the second German Spacelab mission D2 [1], [2]. The Advanced Spaceborne Thermal Emission and Reflection Radiometer (ASTER) on the first NASA spacecraft (Terra) of the Earth Observing System is capable of stereo observations [3]. The design of the multiline array push broom scanner

TABLE I
PARAMETERS OF TLCs ON THE ZY-3 SATELLITE

Characteristics	Forward camera	Nadir camera	Backward camera
Focal length (mm)	1700	1700	1700
Pixel size (mm)	0.010	0.007	0.010
CCD array (pixel)	16300	24530	16300
Swath (km)	52	51	52
Ground resolution (m)	3.2	2.1	3.2

was also adopted by the Systeme Pour l'Observation de la Terre (SPOT5) satellite with two high-resolution stereo (HRS) cameras tilted by $\pm20°$ at a maximum base-to-height ratio of 0.7 and a ground sampling distance (GSD) of 10 m across track and 5 m along track [4], [5]. SPOT5 was the beginning of wide usage of stereo observation satellites in mapping applications. India remote-sensing satellite (IRS)-P5 and the Advanced Land-Observing Satellite (ALOS) are similarly designed. Two independent cameras are integrated on IRS-P5 with tilt angles of $26°$ and $-5°$ looking forward and backward, respectively [6]. The Panchromatic Remote-sensing Instrument for Stereo Mapping (PRISM) sensor on ALOS consists of three independent cameras with forward and backward cameras tilted $23.8°$ and $-23.8°$ from the nadir camera, respectively [7], [8]. After pre- and in-flight calibration, the direct georeferencing accuracy of HRS on SPOT5 is about 35 m [5], whereas those of panchromatic stereo cameras on IRS-P5 and PRISM on ALOS are about 100 m [6] and 30 m [7], [8], respectively.

ZY-3 is the first civilian stereo mapping satellite in China. Its orbit is sun-synchronous tilted at $97.421°$ inclination at the nominal altitude of 506 km with local time at descending node at 10:30 AM. The three-line camera (TLC) sensor on board consists of three independent cameras looking forward, nadir, and backward; the main characteristics of the TLCs on ZY-3 are shown in Table I. The GSD of the nadir image is about 2.1 m, and the forward and backward images are both about 3.2 m, and a ground swath of about 50 km. The forward and backward cameras are tilted $22°$ and $-22°$ from the nadir camera, forming a large base-to-height ratio of 0.8. Three charge-coupled device (CCD) arrays, each of which has 8192 CCD units, are installed on the nadir camera, whereas four CCD arrays, each of which has 4096 CCD units, are installed on the forward and backward cameras. The adjacent CCD arrays are actually installed in two perpendicular planes with no mechanic overlap. However, the designed optical system allows these CCD arrays to have optical overlaps (about 23 pixels in the

Focal plane of the forward and   Focal plane of the nadir camera
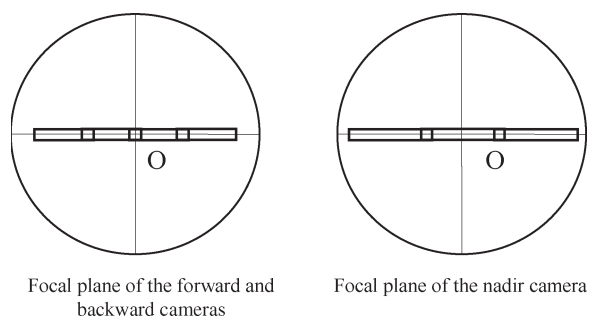backward cameras

Fig. 1.   Designed CCD equivalent position on the focal plane of the three-line sensor.

nadir camera and 28 pixels in both the forward and backward cameras) with their adjacent CCD arrays to assure capturing seamless images. These overlaps are removed in the whole image after preprocessing. The equivalent distribution of CCD arrays on the focal plane is illustrated in Fig. 1, where O is the principal point. High-accuracy GPS receivers, gyroscope units, and star trackers are also integrated on board to measure the instantaneous position and attitude of the satellite, which will be transferred to ground stations together with auxiliary data to be used to perform direct georeferencing. The accuracy of direct georeferencing of ZY-3 imagery has been tested by using the original position and attitude data and laboratorial camera parameters with nine strips of data. All check points are measured from Google Earth. Image point residuals are calculated by forward intersection and then back projection. These image point residuals represent the internal/relative accuracy of TLC sensor in image space. The check points RMSE represents the external/absolute accuracy in object space. According to the test results, the external/absolute accuracy of direct georeferencing before calibration is about 1300 m in plane and 300 m in height, and the internal accuracy is about 200 pixels.

The camera calibration process mainly includes camera alignment angle error correction; camera focal length error correction; lens distortion correction; and whole CCD array rotation, translation, scaling, and bending error corrections. Since the CCD alignment plane of the TLC sensor is divided into a number of sub-CCD arrays, as shown in Fig. 1, there may be alignment errors between different sub-CCD arrays that will cause distortions on an image. These alignments have been calibrated in the laboratory, but they may change after launching; thus, on-orbit geometric calibration is needed.

Many methods have been developed for on-orbit geometric sensor calibration. Sensor mounting alignment with spacecraft and sub-CCD alignment calibration were performed for PRISM on ALOS [7]. During the on-orbit geometric calibration of SPOT5, its sensor alignment, the high-resolution geometrical (HRG) instrument steering mirror off the nadir model, and the HRG/HRS detection lines are calibrated [5]. Boresight misalignment parameters, camera interior orientation parameters, flying direction dependent corrections, height parameters, and datum/coordinate transformation are calibrated during the on-orbit geometric calibration of IRS-P5 [6]; and Mulawa introduced the on-orbit geometric calibration of OrbView-3 [9]. These calibration methods have common points in that they all use high-accuracy ground control points (GCPs) and generally

use a data set from only one strip at one time. Different types of interior orientation parameters (IOPs) may not be distinguishable to each other, which cannot be simultaneously calibrated when a sensor is on orbit. High-accuracy GCPs are usually obtained by field survey or measured on large-scale ortho images and high-accuracy digital elevation model (DEM), which is a costly procedure. The number and distribution of these GCPs are usually limited while dealing with long orbit data. IOPs and exterior orientation parameters (EOPs) are also entangled to each other in the calibration process. Camera calibration will be influenced by EOP errors (i.e., orbit and attitude errors of satellite) and IOP errors.

In this paper, we describe a method using a multistrip data set at the same time during calibration. Medium-accuracy GCPs are obtained by automatic image matching from publicly available reference data Google Earth and shuttle radar topography mission (SRTM). Camera mounting alignment angles, CCD translation, scaling, and sub-CCD arrays alignment are calibrated. Compared with the conventional geometric calibration method discussed in the previous paragraph, our method has the following advantages.

1) Multistrip data sets are simultaneously used. When adequate numbers of strips are involved, the calibration results can be stabilized.
2) Medium-accuracy digital ortho map (DOM) and DEM reference data are used to automatically measure control points, the number of GCPs is largely increased, and the GCPs distribution is pervasive. Therefore, no test field is needed, the cost of calibration is substantially reduced, and the calibration process becomes fully automatic.

After calibration with our method, plenty of experiments have shown that the accuracy of direct georeferencing has been largely improved. The image point residuals RMS of direct georeferencing is less than 1.0 pixel; check point RMSE is about 20 m in plane and 20 m in height. By setting medium-accuracy points as the GCPs and setting high-accuracy points as check points, bundle block adjustment can achieve an accuracy of 10 m in both plane and height. If higher accuracy field points (such as GCPs from Songshan test field) are set as control points, the accuracy can be further improved to about 2–3 m in both plane and height. The overall accuracy is better than that of using a conventional calibration model, which often adopted single strip data at one time and need high-accuracy GCPs. The described calibration method in this paper has been already used in the operational ground data processing system of the ZY-3 satellite.

The succeeding content of this paper is organized in four sections. Section II introduces the trajectory model of the exterior orientation and the geometric calibration model. Section III gives an introduction of the data set used in this paper and demonstrates various experimental results, where the image data of 19 strips are tested. Ten of the strips are involved in camera calibration, and the number of strips simultaneously used in calibration is gradually increased from one to ten. Camera alignment angle errors are calibrated first, and then, the whole CCD array translation and scaling errors and alignment errors between sub-CCD arrays are calibrated. The accuracies

of calibration with different numbers of strips from one to ten are shown, as well as the statistical results and analysis of direct georeferencing and bundle block adjustment with different calibrated parameters. In Section IV, validations of the calibration results with our method on ZY-3 TLC imagery are discussed. The conclusions and recommendations of this paper are provided in the final section.

II. MATHEMATICAL MODEL

A. Sensor Model

A trajectory model is necessary in order to model the real orbit during bundle block adjustment with linear imagery. Jung and Bethel applied a stochastic model based on the first-order Gauss–Markov operator [10]; others used the Kepler orbit model [11], [12]. The quadratic polynomial model, the systematic error compensation model, the piecewise polynomial model, and the orientation image model were also adopted by researchers [13]. Among them, the systematic error compensation model and the orientation image model have been the most commonly applied thus far. Since the cloud and ground object characters are unknown and unforeseen and the distribution of image texture is usually unpredictable, GCPs and pass points are all automatically matched from reference data; thus, the number and distribution of GCPs and pass points will be influenced by clouds, bodies of water, desert, plants, and areas that may have low contrast. If the orientation image model is adopted, when the orientation images have fallen into the exact area that has no GCP and pass point, bundle block adjustment may not converge, and the results may be very unstable. The piecewise polynomial model is not a proper model in this case either. On the other hand, its accuracy of orbit determination is high; the satellite real-time position errors are examined in the next section. In this case, we could adopt the more stable trajectory model, i.e., the systematic error compensation model. Many additional experiments verified that considerable accuracy could be obtained by adopting the systematic error compensation model and needed only to compensate for the constant error of the orbit and the attitude observations data. The data processing system of the ZY-3 satellite also uses this model.

The systematic error compensation model lumps all EOP errors at the sensor mounting interface, which is expressed in the superposition of systematic errors over the real-time sensor position and attitude observations, i.e.,

$$
\begin{aligned}
Xs &= Xs_0 + \Delta Xs \\
Ys &= Ys_0 + \Delta Ys \\
Zs &= Zs_0 + \Delta Zs \\
\varphi &= \varphi_0 + \Delta\varphi \\
\omega &= \omega_0 + \Delta\omega \\
\kappa &= \kappa_0 + \Delta\kappa
\end{aligned}
\tag{1}
$$

where Xs, Ys, Zs, φ, ω, and κ are the satellite position and attitude; and Xs_0, Ys_0, Zs_0, φ_0, ω_0, and κ_0 are the on-board observations of the position and attitude of the sensor. ΔXs, ΔYs, ΔZs, $\Delta\varphi$, $\Delta\omega$, and $\Delta\kappa$ are the systematic errors of the position and attitude of the sensor. These are all time dependent. In this paper, we treat the systematic errors as time-independent constants. As shown in Section III, bundle block adjustment using these parameters achieved good accuracy. Temporal trends will be tracked, and possible corrections may be needed as data accumulate.

B. Camera Geometric Calibration Model

It is known that EOP and IOP errors are correlated in the process of calibration. Calibration of one set of parameters may absorb another set, or vice versa. The EOPs and their systematic errors are expressed in (1) and will be further expressed in "connection" with IOPs. The IOPs include the camera focal length, lens distortion, CCD translation, rotation, scaling, bending on the focal plane, and the misalignment of sub-CCD arrays with each other. Errors caused by lens distortion and CCD bending were small and negligible, and these errors could not be identified by the GCPs with medium accuracy. Camera alignment angle errors with respect to the spacecraft that have large effects on the georeferencing accuracy will be calibrated first. CCD scaling errors along the CCD array and the sub-CCD arrays' alignment error with each other also needed to be calibrated. The camera focal length error was related to the CCD scaling error and constant error in the EOP. To avoid the relativity, only the CCD scaling errors were calibrated. As for the ZY-3 TLC sensor, after examining a large number of imagery, we concluded that the CCD alignment errors of the imagery collected by the forward and backward cameras were small enough to be neglected. However, the CCD alignment errors of the nadir camera need to be calibrated. Since the sub-CCD arrays in nadir cameras are longer than those in forward and backward cameras, larger distortion may occur during manufacturing. In addition, three sub-CCD arrays may have different systematic errors; thus, sub-CCD array geometric calibration also may be necessary. CCD rotation and translation errors are entangled with camera misalignment with the spacecraft and are inseparable from each other. Therefore, the calibration of CCD rotation and translation is absorbed in the calibration of camera alignment angle and translation with the spacecraft. The translation values between the cameras and the spacecraft were calibrated in the laboratory, the translation errors caused by launching usually are much smaller, considering the 2.1-m GSD, and the camera translation error is also entangled with camera alignment angle error with the spacecraft; thus, the camera translation errors with the spacecraft are neglected in this paper. However, CCD array translation error calibration is still performed after the calibration of camera alignment angle to correct a few remained errors.

The calibration of the camera mounting errors in alignment angle was described in the succeeding equations along with the whole CCD array translation error, the whole CCD array scaling error, and the alignment errors of sub-CCD arrays.

1) Sensor Alignment Calibration: A traditional collinearity equation can be represented as (2) after the introduction of the sensor misalignment angle with respect to the spacecraft, i.e.,

$$
\begin{bmatrix} Xs - X \\ Ys - Y \\ Zs - Z \end{bmatrix} = \lambda R_{\text{obj2orb}} R_{\text{orb2sat}} R_{\text{sat2cam}} \begin{bmatrix} x \\ y \\ -f \end{bmatrix}
\tag{2}
$$

where Xs, Ys, and Zs are the coordinates of the perspective center; X, Y, and Z are the coordinates of the object point; x and y are the coordinates of the corresponding image point; f is the focal length; λ is the scaling coefficient; R_{obj2orb} is the rotation matrix from the orbit coordinate system to the object coordinate system; R_{orb2sat} is the rotation matrix from the satellite coordinate system to the orbit coordinate system; and R_{sat2cam} is the rotation matrix from the camera coordinate system to the satellite coordinate system.

As for the ZY-3 data, since the rotation matrix from the satellite coordinate system direct to the object coordinate system was preprocessed, the given attitude data are the rotation angles from the spacecraft coordinate system direct to the object coordinate system. The rotation matrix from the camera to the spacecraft consists of three mounting angles. Thus

$$R_{\mathrm{obj2sat}} = R_{\mathrm{obj2orb}} R_{\mathrm{orb2sat}} = R(\omega) R(\varphi) R(\kappa)$$
$$R_{\mathrm{sat2cam}} = R(p + \Delta p) R(l + \Delta l) R(k + \Delta k) \qquad (3)$$

where φ, ω, and κ are the rotation angles from the spacecraft to the object coordinate system; p, l, and k are the laboratory-calibrated values of the three rotation angles from the camera to the spacecraft; and Δp, Δl, and Δk are the errors of p, l, and k, respectively; they are also the only unknown parameters of the sensor alignment calibration.

Combining (2) and (3) yields

$$\begin{bmatrix} Xs - X \\ Ys - Y \\ Zs - Z \end{bmatrix} = \lambda R_{\mathrm{obj2sat}} R_{\mathrm{sat2cam}} \begin{bmatrix} x \\ y \\ -f \end{bmatrix}$$
$$= \lambda R(\omega) R(\varphi) R(\kappa) R(p + \Delta p) R(l + \Delta l)$$
$$\times R(k + \Delta k) \begin{bmatrix} x \\ y \\ -f \end{bmatrix}. \qquad (4)$$

In (4), Δp, Δl, and Δk are the only calibration parameters of the sensor alignment calibration.

Note that, although the errors in rotational angles are ascribed to the sensor mounting interface, their corrections during on-orbit geometric calibration absorb the rotational angle error corrections in a whole train of coordinate transformation matrices, such as the star tracker mounting interface with spacecraft and the camera CCD array orientation with camera body coordinates.

2) CCD Array Alignment Calibration: The mathematical model of whole CCD array calibration is as follows:

$$\begin{bmatrix} Xs - X \\ Ys - Y \\ Zs - Z \end{bmatrix} = \lambda R_{\mathrm{obj2sat}} R_{\mathrm{sat2cam}} \begin{bmatrix} x + \Delta x \\ y + \Delta y \\ -f \end{bmatrix} \qquad (5)$$

$$\Delta x = x_0$$
$$\Delta y = y_0 + y_1 c \qquad (6)$$

where x_0 is the CCD array translation error along track; y_0 and y_1 are the CCD array translation and scaling errors across track; and c is the pixel column ID in the whole image.
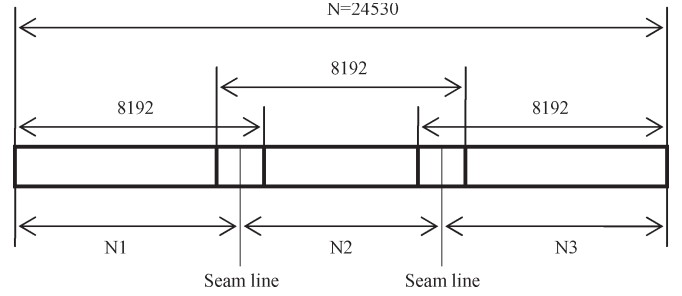

Fig. 2. Overlaps of CCD arrays in the nadir camera. The middle CCD is shifted in the y-direction against N1 and N3 (no mechanical overlap possible).

The mathematical model of the sub-CCD array calibration in the nadir camera is as follows:

$$\Delta x = \begin{cases} x_0 & 0 < c < N_1 \\ x_1 & N_1 < c < N_1 + N_2 \\ x_2 & N_1 + N_2 < c < N \end{cases}$$

$$\Delta y = \begin{cases} y_0 + y_1 c & 0 < c < N_1 \\ y_2 + y_3 c & N_1 < c < N_1 + N_2 \\ y_4 + y_5 c & N_1 + N_2 < c < N \end{cases} \qquad (7)$$

where x_0, x_1, and x_2 are the translation errors along track of the three sub-CCD arrays of the nadir camera; y_0, y_1, y_2, y_3, y_4, and y_5 are the translation and scaling errors across track of the three sub-CCD arrays of the nadir camera; c is the CCD column ID in the whole CCD array; N_1 and N_2 are the actual pixel numbers captured by the first and second CCD arrays, respectively, in the whole mosaic image, as shown in Fig. 2; N is the pixel number of the whole image captured by the nadir camera; and c is the pixel column ID in the whole image.

This paper discusses calibration and correction of sub-CCD arrays translation and scaling errors across track since the alignment of the sub-CCD arrays was fairly accurate along track and the translation errors of each sub-CCD array were already calibrated in the whole CCD array calibration process.

III. EXPERIMENTS AND ANALYSIS

A. Weight Strategy

The weights of the observations of position and attitude were fixed during adjustment. The initial weights of the image points were set at 1.0, and the weights of others were set to be the square of the ratio of its accuracy against the accuracy of the image point observations. After iteration during adjustment, the weight of each image point was recalculated according to its residuals. If the residuals were smaller than a threshold value (such as 1 pixel), the relative image point weight will remain unchanged.

B. Experimental Data Set

A total of 19 strips of ZY-3 TLC imagery was tested, and the average length of these strips was about 3000 km. The ground coverage (an extensive portion of China) is shown in Fig. 3. The position and attitude data of the perspective center were preprocessed before calibration. We randomly examined a data set of one strip from all of the 19 strips, and the real-time
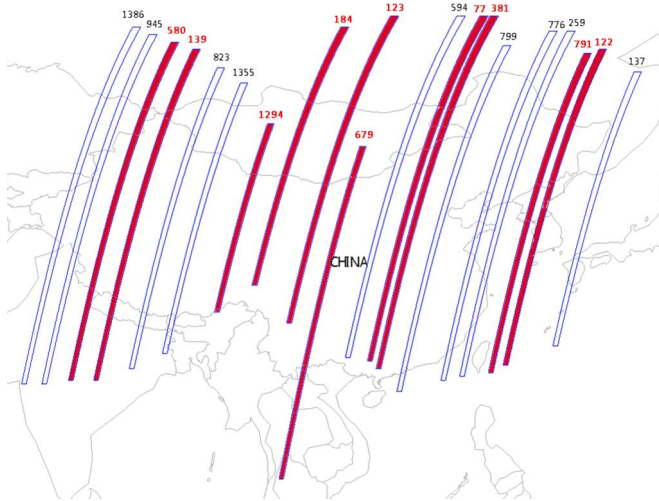
Fig. 3.   Ground coverage of all test data. The numbers were orbit ID (ten strips, shown as solid area, were involved in multistrip calibration).

satellite position observations were compared with postprocessed positions; the postprocessed positions are calculated by a differential positioning approach using original carrier phase observations of GPS receivers on board and base stations on the ground, the accuracy of which was claimed to be about 0.05 m [15] and can be assumed as true value of satellite positions. The differences between the real-time satellite position observations and the postprocessed position data are represented as errors of the real-time satellite position observations, i.e., the EOP positional errors where the EOP positions are influenced by attitude errors. The results are illustrated in Fig. 4. The maximum absolute EOP positional error is about 5.0 m, less than 2.0 GSD; this is a considerable high accuracy. All pass points and medium-accuracy control points were automatically matched from publicly available reference data Google Earth and SRTM. The accuracy of these GCPs is assessed to be about 20 m in plane and 15 m in height. High-accuracy GCPs are all obtained from Songshan test field and Pinghu area. The Songshan test field is located in Henan province in China; it is built to calibrate airborne optical sensors; the Pinghu area is located in Zhejiang province in China; it is not a test field, but the $1:10\,000$ topographic ortho images and DEM of this area are available. GCPs from the Songshan test field are field control points, which have centimeter-level accuracy, and the accuracy of GCPs from Pinghu area is about 3 m in plane and 5 m in height. Image point residuals in this paper are calculated by forward intersection and back projection; they can represent the internal/relative accuracy of TLC sensor in image space, whereas the check points RMS can represent the external/absolute accuracy in object space. The control points matched from reference data scene by scene; and they are very dense, with about 5000 points per scene (50 km × 50 km). The average number of control points for a strip is about $300\,000$ since the average length of the test strips is about 3000 km (about 60 scenes). All bundle block adjustment processes were performed under the WGS84 coordinate system, but check point RMSE was transferred to the tangential plane coordinates and the geodetic height system.
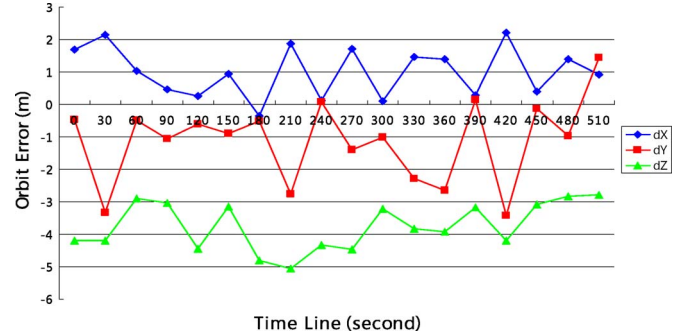

Fig. 4.   Difference of the real-time satellite position data and the postprocessed position data.

C. Camera Alignment Angle Calibration

The number of strips that were used in calibration was gradually increased from one to ten; the camera alignment angle errors Δp, Δl, and Δk (which are shown as Pitch, Roll, and Yaw in Fig. 5) were calibrated.

As shown in Fig. 5, the corrections of alignment angles from the camera to the spacecraft show a trend of stabilization as the number of strips is gradually increased. That is to say, the corrections approach their expected values in the probability sense. When only one strip data was used, the uncertainty in the corrections of the errors on calibration was very large, a result that was much different from calibration using multistrip data. At least three strips of data were needed to reduce the uncertainty in the corrections in the orbit position error and the attitude errors in pitch and roll angles. However, the yaw angle parameter correction was still unstable, which was probably due to the fact that the yaw angle error had less influence on the accuracy of the georeferencing than the pitch and roll angles.

D. Whole CCD Array Calibration

Using translation parameters x_0 along track and y_0 across track, the scaling parameters y_1 across track were calibrated as the number of strips was gradually increased from one to ten.

As demonstrated in Fig. 6, when the number of strips used in calibration was no more than six, the calibration results were quite unstable, which indicates that the uncertainties of corrections are still high. As the number of strips involved in calibration was increased, however, the parameters after calibration were more stabilized and approached a certain value, which might be the true value of the parameters. Translation parameter x_0 along track converged to zero since the translation error was already absorbed in the sensor alignment angle calibration in the last step. Translation parameter y_0 across track had a different situation in that some translation errors remained across track after calibration in the last step, most likely due to the existing scaling errors across track. Scaling parameter y_1 across track converged to a certain value, which means that the scaling error did exist across track. At least six strips were confirmed to be needed to reach the expected correction values.
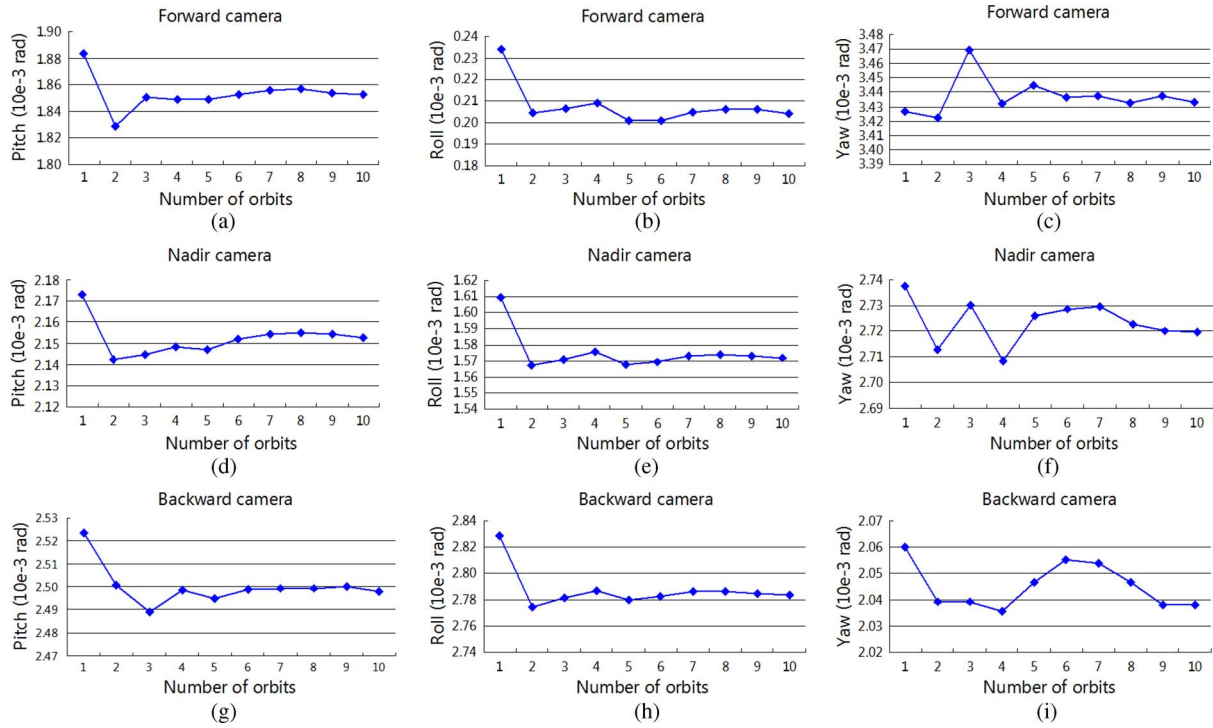
Fig. 5. Camera alignment angle correction results as the number of strips involved increased from one to ten.
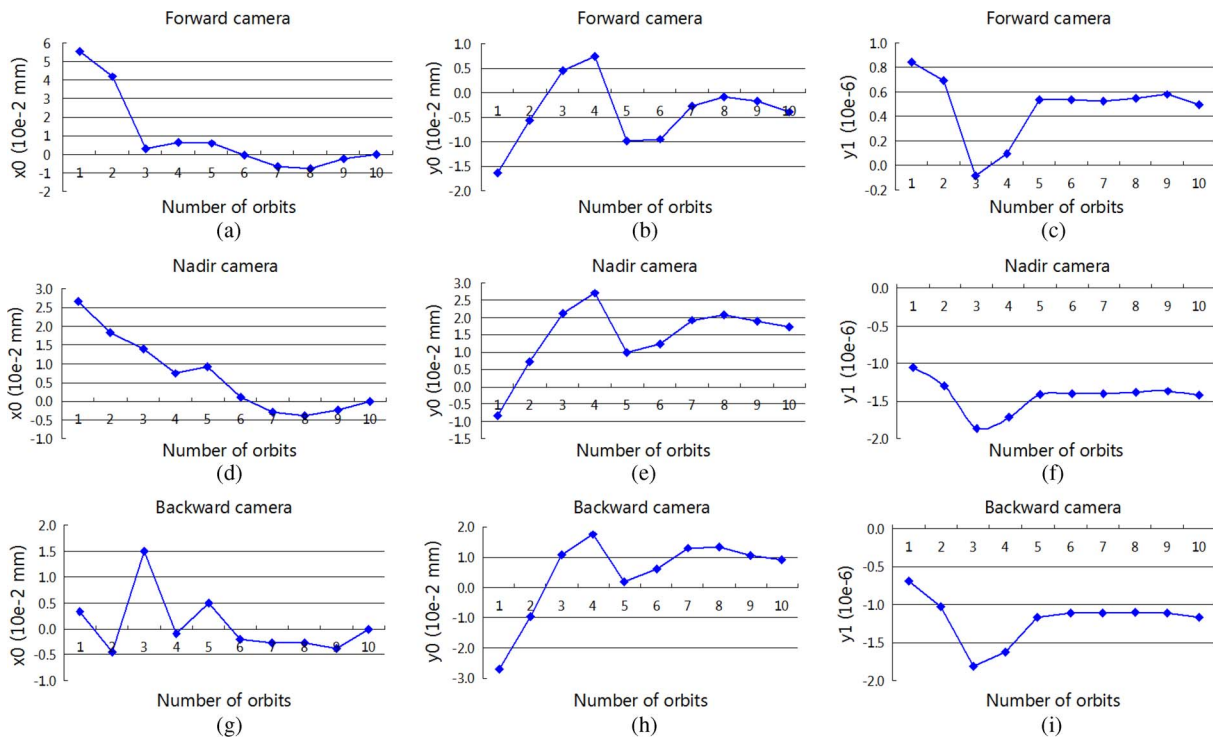

Fig. 6. Whole CCD array calibration results as the number of orbits involved increased from one to ten.

E. Sub-CCD Array Alignment Calibration

After the whole CCD array calibration was performed, the translation and scaling parameters of the three sub-CCD arrays were calibrated according to (7). All of the ten data strips were simultaneously processed.

As shown in Fig. 7(a) and (b), slight CCD alignment errors still exist along track, but significant CCD alignment errors exist across track after camera alignment angle calibration in previous. After the whole CCD array calibration, translation and scaling errors are almost corrected, and the sub-CCD
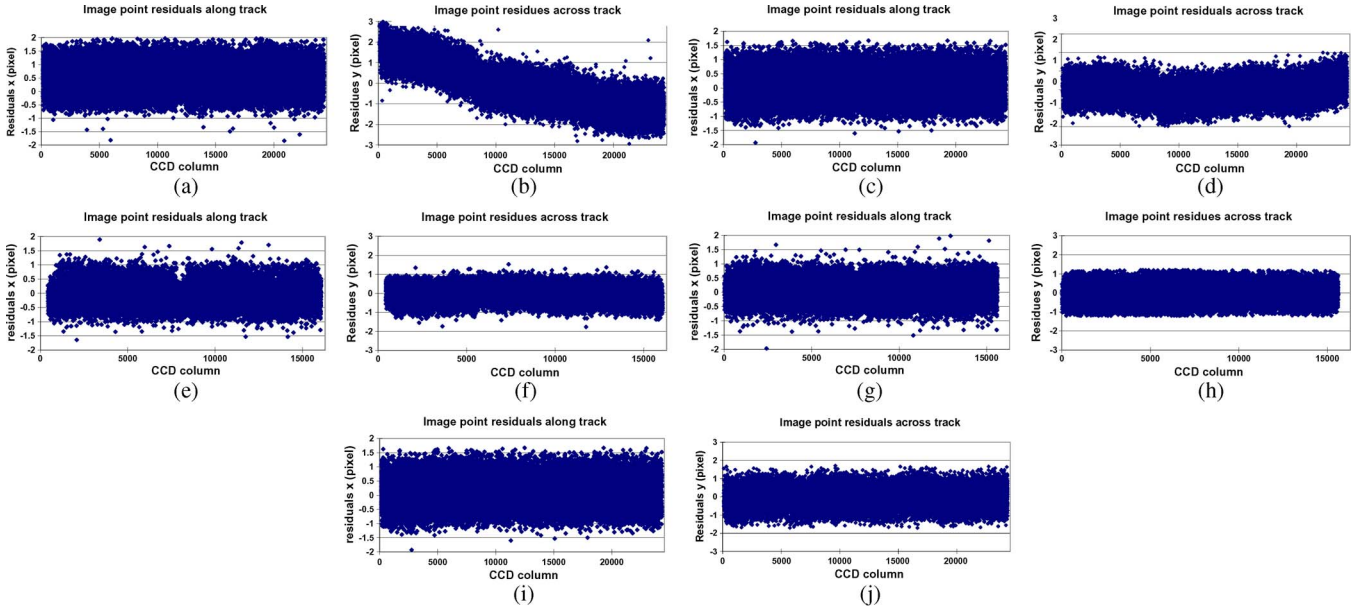
Fig. 7. Image point residuals of different process schemes. (a) and (b) Results along track and across track before any CCD calibration for the nadir camera. (c) and (d) After whole CCD array calibration for the nadir camera. (e) and (f) After whole CCD array calibration for the forward camera. (g) and (h) After whole CCD array calibration for the backward camera. (i) and (j) After whole CCD array and sub-CCD array calibration for the nadir camera.

TABLE II
RESULTS OF BUNDLE BLOCK ADJUSTMENT AFTER CALIBRATION WITH DIFFERENT METHODS

Calibration methods	RMS of image point residuals		Max image point residuals		RMSE of check point		Max check point errors	
	x (pixel)	y (pixel)	x (pixel)	y (pixel)	XY (m)	H (m)	XY (m)	H (m)
No-CCD-Calibration	0.30	0.81	2.47	-2.47	14.67	7.77	56.25	-31.42
Whole-CCD-Calibration	0.30	0.54	1.79	-1.80	14.38	7.84	51.94	31.06
Whole and Sub-CCD-Calibration	0.30	0.52	1.71	-1.72	14.35	7.76	51.04	31.87

array alignment errors along track for the nadir camera were already negligible after the whole CCD alignment calibration, as shown in Fig. 7(c). Similar results were obtained for the forward and backward cameras, as shown in Fig. 7(e) and (g); furthermore, sub-CCD array alignment errors across track for these two cameras were also negligible, as shown in Fig. 7(f) and (h). However, alignment errors between the sub-CCD arrays across track for the nadir camera needed further calibration, as demonstrated in Fig. 7(d). After the sub-CCD array calibration, these errors were finally corrected, and all image point residuals were randomly distributed, as shown in Fig. 7(j) and Table II. It was shown that best results could be achieved by bundle adjustment with whole and sub-CCD array calibration.

IV. VALIDATION OF THE CALIBRATION RESULT

A. Direct Georeferencing and Bundle Block Adjustment With Calibrated Parameters

To fully evaluate the accuracy levels of different calibration methods, a data set of 19 strips was used to perform direct georeferencing and bundle block adjustment with different IOPs. Systematic error compensation models, as aforementioned, were applied as sensor models in bundle block adjustment.

Each of the strips has a strip ID, which is numbered from 1 to 19, in turn, as the orbit ID increasing by time. First, the results of single strip and multistrip calibration were compared, and the results with and without CCD alignment error calibration were also determined. Then, high-accuracy object points were used to check the real calibration accuracy of all these methods in bundle block adjustment. All of the experiment schemes with different IOPs calibration methods (number of involved strips, calibrated parameters, and control point accuracy levels) and processes are listed in Table III.

1) Comparison of the Single Strip and Multistrip Calibration, With or Without CCD Alignment Error Calibration: In this experiment, all check points and control points are medium-accuracy GCPs in both bundle block adjustment and direct georeferencing. In Fig. 8, SSR_DG (blue diamond) and MSR_DG (pink small square) represent the direct georeferencing accuracies of single strip and multistrip calibration, respectively. It is clear that the results of multistrip calibration are much better than the single strip calibration results for most strips, except strip 1. The first strip was used in the single strip calibration process; thus, the calibrated IOP had compensated for the EOP errors in strip 1, whereas the results of multistrip calibration were not. Thus, the accuracy of direct georeferencing in strip 1 was better than multistrip calibration, but only for strip 1.

TABLE III
DIFFERENT IOP CALIBRATION METHODS AND PROCESS SCHEMES

| Scheme	Number of involved strips in calibration	Calibrated parameters in calibration	Control point accuracy level in calibration	Process
SSR_DG	Single(1)	Misalignment angle	medium	Direct georeferencing
MSR_DG	Multi(10)	Misalignment angle	medium	Direct georeferencing
MSRC_DG	Multi(10)	Misalignment angle and CCD misalignment parameters	medium	Direct georeferencing
HPG_DG	Single(1)	Misalignment angle and CCD misalignment parameters	high	Direct georeferencing
MSR_ADJ	Multi(10)	Misalignment angle	medium	Bundle block adjustment with systematic error compensation model
MSRC_ADJ	Multi(10)	Misalignment angle and CCD misalignment parameters	medium	Bundle block adjustment with systematic error compensation model
HPG_ADJ	Single(1)	Misalignment angle and CCD misalignment parameters	high	Bundle block adjustment with systematic error compensation model
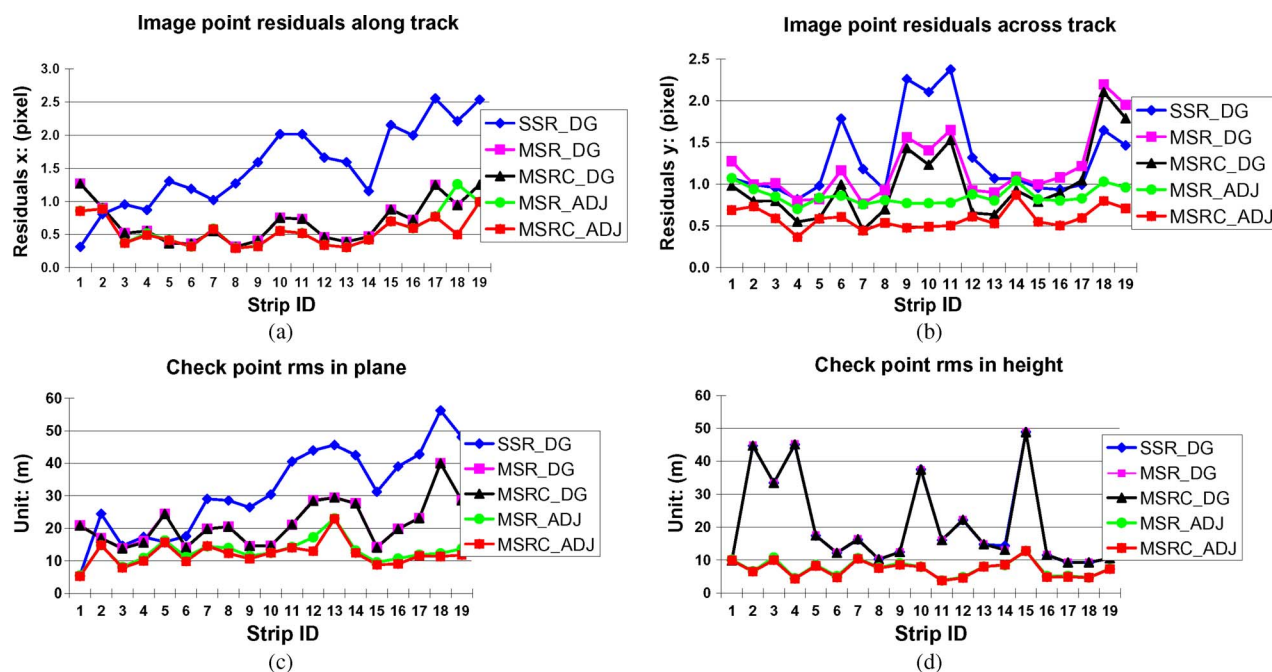
Fig. 8. Different results of processes with different strategies.

The image point residuals containing CCD alignment calibration (MSRC_DG and MSRC_ADJ shown in Fig. 8 as black triangle and big red square, respectively) were much better than the calibration result that calibrated only the misalignment angles (MSR_DG and MSR_ADJ shown in Fig. 8 as small pink square and green circle); but the object absolute accuracy turned was the same, which was likely due to the CCD alignment error having very little effect on the object absolute accuracy.

Comparing MSR_DG (small pink square) and MSRC_DG (black triangle) with MSR_ADJ (green circle) and MSRC_ADJ (red big square), bundle block adjustment accuracy was much better because the accuracy of the direct georeferencing was influenced by the EOP errors. After bundle block adjustment, which compensated for the constant errors of the position and attitude observations, which are known as EOP errors, the

accuracy levels were greatly improved to about 0.5 pixel of internal accuracy and 10 m of external accuracy. These results indicate that the EOP errors were almost corrected, which also indicates that multistrip calibration can reduce the uncertainties caused by EOP errors.

As for the ZY-3 imagery, considerable accuracy was obtained by only compensating for the constant errors of the position and attitude observations, which verified the statement in the preceding section.

2) Result of Bundle Block Adjustment Using High-Accuracy Points as Both GCPs and Check Points: Using high-accuracy points as GCPs and check points, three groups of IOPs, which are calibrated by different methods, are used as fixed values. The results of bundle block adjustment with the systematic error compensation model applied as the sensor model are listed in Table IV.

TABLE IV
ACCURACY OF BUNDLE BLOCK ADJUSTMENT WITH HIGH-ACCURACY GCPS AND CHECKED BY HIGH-ACCURACY CHECK POINTS

Test areas	IOP calibration method	GCP number	Check point number	RMS of image point residuals		Max image point residuals		RMSE of check point		Max check point errors	
				x (pixel)	y (pixel)	x (pixel)	y (pixel)	XY (m)	H (m)	XY (m)	H (m)
Songshan	SSR_ADJ	3	75	1.42	0.86	-2.60	2.99	1.83	4.06	4.79	-7.53
	MSRC_ADJ	3	75	0.22	0.31	0.71	0.95	1.32	1.70	3.46	4.82
	HPG_ADJ	3	75	0.26	0.32	0.73	-0.97	1.40	1.65	4.22	-4.02
Pinghu	SSR_ADJ	10	320	1.40	0.92	2.76	-2.95	2.53	5.00	6.76	-9.09
	MSRC_ADJ	10	320	0.56	0.60	1.46	1.46	1.47	2.58	5.19	5.33
	HPG_ADJ	10	320	0.63	0.67	1.62	2.00	2.02	2.48	5.65	5.83

As shown in Table IV, bundle block adjustment using the systematic error compensation model with a few high-accuracy control points in the Songshan test field can achieve remarkable accuracies of about 1.3 m in plane and 1.7 m in height, which also indicates that the imagery of the ZY-3 satellite is capable of producing high-accuracy ortho images or other geometric products. If the 1 : 10 000 scale fundamental geospatial data are used as control points, the best accuracy of bundle adjustment in the Pinghu test area is on the level of 2.0 m in plane and 2.5 m in height.

B. Digital Surface Model (DSM) and DOM Performance

ZY-3 is a satellite aimed to produce 1 : 50 000 scale topographic maps. The geometric accuracies of the onboard sensors are the main concern. According to the Chinese national standard of 1 : 50 000 scale topographic mapping, the accuracy requirements are 25 m in plane; and 3, 5, and 8 m in height in flat, hilly, and mountainous areas, respectively. The calibration method in this paper had been used in the operational ground data processing system of the ZY-3 satellite, and will be used in future if new calibration is necessary. After calibration with multistrip data using medium-accuracy GCPs and bundle block adjustment using high-accuracy GCPs, a rational function model of each standard scene was generated [14] for DSM and DOM generation with sensor independent technologies. High-accuracy field points of the Songshan area were used to check the automatically and operationally generated DSM and DOM with ZY-3 TLC imagery.

Three scenes of DSM and DOM products in the Songshan test field were shown in Fig. 9, where DSM was shown with a pseudo-color image. A total of 198 GCPs was used to check the accuracies of the DSM and DOM products. In Table V, the accuracies of automatically generated DSM and DOM are listed when compared with the available high-accuracy ground points. As can be seen, the accuracies of DSM and DOM products met the requirements of 1 : 50 000 scale topographic mapping.

V. CONCLUSION

A new on-orbit calibration method has been described in this paper to calibrate the TLC sensor on China's first commer-
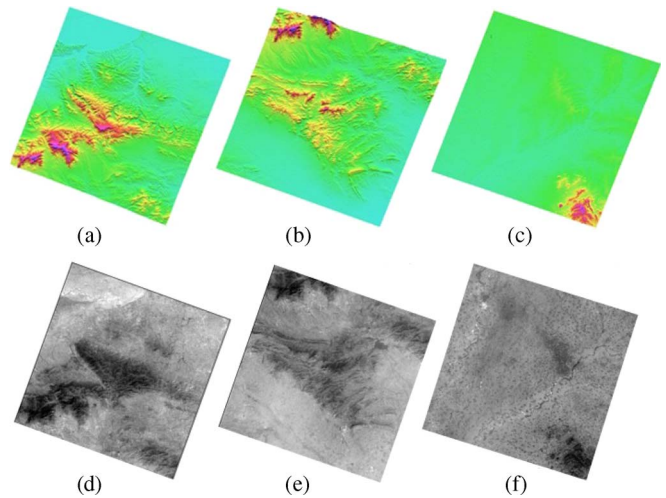

Fig. 9. Three DSM and DOM products of the Songshan area (DSM resampling distance: 25 m; DOM resampling distance: 2.5 m).

cial stereo mapping satellite, the ZY-3 satellite. Ten strips, at most, were simultaneously processed in calibration, medium-accuracy ortho images and DEM were used as reference data, and control points were automatically matched from these publicly available reference data. Camera alignment angles to the spacecraft, whole CCD array translation, scaling parameters, and sub-CCD arrays alignment were calibrated. All of the 19 data strips were used to check the parameters calibrated by different methods, and the results were analyzed and compared. Numerous experiments demonstrated that multistrip calibration can efficiently reduce the influence caused by EOP errors during on-orbit geometric calibration, that only medium-accuracy control points should be used in calibration, and that the accuracy of multistrip calibration is better than single strip calibration. Automatic control point matching also reduced the cost of a test field, which is indispensable in traditional calibration. In addition, the entire calibration process was fully automatic, which substantially improved its efficiency.

1) Since the IOP and EOP are intertwined in the on-orbit geometric calibration process, the EOP errors have effects on the IOP calibration. Multistrip calibration can efficiently reduce the uncertainties in the corrections in

TABLE V
HEIGHT ACCURACY OF DSM OF SONGSHAN AREA CHECKED BY HIGH-ACCURACY FIELD POINTS (UNIT: IN METERS)

Scene ID	Terrain type	Number of check points	Accuracies of DSM				Accuracies of DOM		
			RMS (m)	Mean (m)	Max (m)	Min (m)	RMS (m)	Max (m)	Min (m)
0063	Mountain & Hill	106	3.92	0.57	17.21	-7.75	3.12	8.53	0.37
0064	Mountain & Hill	58	3.37	2.12	9.57	-6.33	2.76	4.66	0.68
0068	Flat	34	2.36	1.40	5.51	-2.66	3.33	5.57	0.47

the orbit position errors and attitude errors. As the number of strips involved in calibration is gradually increased, the calibrated parameters converge to certain values, and the results become more stable.

2) After calibrating the camera misalignment angles to the spacecraft, the whole CCD array translation, the scaling errors, and the sub-CCD arrays alignment errors with multistrip data (at most, ten strips) using medium-accuracy GCPs, the accuracy of direct georeferencing can achieve the internal accuracies of about 0.3–0.5 pixels along track and no more than 1.0 pixel across track and external accuracies of about 6 m in plane and 11 m in height. The accuracies of the bundle block adjustment with the systematic error compensation model using medium-accuracy GCPs are improved to about 4 m in plane and 3 m in height. Accuracies of about 1.3 m in plane and 1.7 m in height can be achieved by using high-accuracy field GCPs in the Songshan test field. However, more high-accuracy global test data sets are needed to verify the global direct georeferencing and bundle block adjustment performance.

3) Alignment errors along track of the sub-CCD arrays in the nadir camera are too small to be identified by medium-accuracy GCPs, but the errors across track can be clearly seen. After sub-CCD arrays misalignment calibration, these errors across track are almost corrected.

4) Considerable accuracy can be achieved by simply compensating for the constant parameters of the position and attitude observations.

5) This new calibration method does not need any test field or high-accuracy GCPs. Only medium-accuracy ortho images and DEM are needed, which can be obtained from public data throughout the world (e.g., Google Earth, MapWorld, Enhanced Thematic Mapper, SRTM, ASTER, etc.). Thus, this method can substantially decrease the high cost of test field construction and maintenance; and a GCP automatic matching system instead of the traditional artificial identification method can make the entire calibration process fully automatic, which could significantly improve its efficiency.

6) Accuracy of automatically and operationally generated DSM and DOM products with ZY-3 TLC imagery can basically meet the requirements of 1 : 50 000 scale topographic mapping.

More data are needed to verify the effectiveness and stability of the introduced method, and more high-accuracy points are needed to verify the accuracy of multistrip calibration.

REFERENCES

[1] H. Ebner, O. Hofmann, W. Kornus, F. Muller, and G. Strunz, "A simulation study on point determination using MOMS-02/D2 imagery," *Photogramm. Eng. Remote Sens.*, vol. 57, no. 10, pp. 1315–1320, 1991.

[2] H. Ebner, W. Konus, and T. Ohlhof, "A simulation study on point determination for the MOMS-02/D2 space project using an extended functional model," *Int. Arch. Photogramm. Remote Sens.*, vol. 29, pt. B4, pp. 458–464, 1992.

[3] K. Thome, K. Arai, S. Hook, H. Kieffer, H. Lang, T. Matsunaga, A. Ono, F. Palluconi, H. Sakuma, P. Slater, T. Takashima, H. Tonooka, S. Tsuchida, R. M. Welch, and E. Zalewski, "ASTER preflight and inflight calibration and the validation of level 2 products," *IEEE Trans. Geosci. Remote Sens.*, vol. 36, no. 4, pp. 1161–1172, Jul. 1998.

[4] L. Zhang and J. X. Zhang, "Block adjustment with sparse GCPs and SPOT-5 HRS imagery for the project of West China topographic mapping at 1 : 50 000 scale," in *Proc. Int. Workshop Earth Observ. Remote Sens. Appl.*, 2008, pp. 1–7.

[5] E. Breton, A. Bouillon, R. Gachet, and F. Delussy, "Pre-flight and in-flight geometric calibration of SPOT5 HRG and HRS images," in *Proc. Pecora 15/Land Satellite Inf. IV/ISPRS Commission I/FIEOS*, Denver, CO, 2002.

[6] P. V. Radhadevi, "In-flight geometric calibration of fore and aft cameras of CARTOSAT-1," in *Proc. Euro-Calibration Orient. Workshop Inst. Geomatics*, Castelldefeis, Spain, 2008.

[7] J. Takaku and T. Tadono, "PRISM on-orbit geometric calibration and DSM performance," *IEEE Trans. Geosci. Remote Sens.*, vol. 47, no. 12, pp. 4060–4073, Dec. 2009.

[8] R. Lei, D. Z. Fan, C. B. Liu, and Q. H. Ma, "Systematic error analysis of direct georeferencing for ALOS PRISM imagery," *J. Geomat. Sci. Technol.*, vol. 28, no. 5, pp. 356–364, May 2011.

[9] D. Mulawa, "On-orbit geometric calibration of the OrbView-3 high resolution imaging satellite," *Int. Arch. Photogramm. Remote Sens. Spatial Inf. Sci.*, vol. 35, pt. B1, pp. 1–6, 2004.

[10] W. J. Jung and J. S. Bethel, "Stochastic modeling and triangulation for an airborne three-line scanner," *Int. Arch. Photogramm. Remote Sens. Spatial Inf. Sci.*, vol. 37, pt. B1, pp. 653–656, 2008.

[11] P. Michalis and I. Dowman, "A generic model for along-track stereo sensors using rigorous orbit mechanics," *Photogramm. Eng. Remote Sens.*, vol. 74, no. 3, pp. 303–309, Mar. 2008.

[12] I. Jeong and J. S. Bethel, "A study of trajectory models for satellite image triangulation," *Photogramm. Eng. Remote Sens.*, vol. 76, no. 3, pp. 265–276, Mar. 2010.

[13] Y. J. Zhang, M. T. Zheng, and T. Ke, "Triangulation of spaceborne three-line array imagery with different sensor models," in *Proc. ASPRS Annu. Conf.*, Milwaukee, WI, 2011.

[14] Y. J. Zhang, Y. H. Lu, L. Wang, and X. Huang, "A new approach on optimization of the rational function model of high resolution satellite imagery," *IEEE Trans. Geosci. Remote Sens.*, vol. 50, no. 7, pp. 2758–2764, Jul. 2012.

[15] P. Hèroux and J. Kouba, "GPS precise point positioning using IGS orbit products," *Phys. Chem. Earth*, vol. 26, no. 6–8, pp. 573–578, 2001.
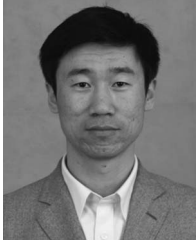
Yongjun Zhang was born in 1975. He received the B.S., M.S., and Ph.D. degrees from Wuhan University, Wuhan, China, in 1997, 2000, and 2002, respectively.

He is currently a Professor of photogrammetry and remote sensing with the School of Remote Sensing and Information Engineering, Wuhan University. His research interests include space, aerial and low-altitude photogrammetry, image matching, combined bundle adjustment with multisource data sets, 3-D city reconstruction, and industrial inspection.
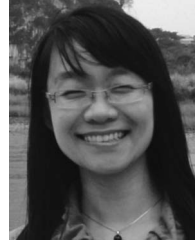
Yihui Lu was born in 1987. She received the B.S. degree from Shandong University, Jinan, China, in 2009. She is currently working toward the Ph.D. degree in the School of Remote Sensing and Information Engineering, Wuhan University, Wuhan, China.

Her research interests include satellite remote sensing and image matching.
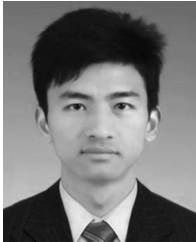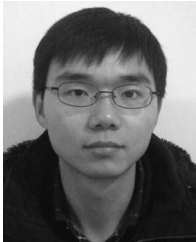
Maoteng Zheng was born in 1987. He received the B.S. degree from Wuhan University, Wuhan, China, in 2009. He is currently working toward the Ph.D. degree in the School of Remote Sensing and Information Engineering, Wuhan University.

His research interests include space and aerial photogrammetry and combined bundle adjustment with multisource data sets.

Xiaodong Xiong was born in 1987. He received the B.S. degree from Wuhan University, Wuhan, China, in 2009. He is currently working toward the Ph.D. degree in the School of Remote Sensing and Information Engineering, Wuhan University.

His research interests include Light Detection And Ranging data processing and aerial photogrammetry.

Jinxin Xiong was born in 1987. He received the B.S. degree from The People's Liberation Army Information Engineering University, Zhengzhou, China, in 2008. He is currently working toward the Ph.D. degree in the School of Remote Sensing and Information Engineering, Wuhan University, Wuhan, China.

His research interests include space and aerial photogrammetry and combined multiview matching algorithm with multisource imagery.